



Verification of image quality and quantification in whole-body positron emission tomography with continuous bed motion

Hideo Yamamoto¹ · Shota Takemoto¹ · Akira Maebatake¹ · Shuhei Karube¹ · Yuki Yamashiro¹ · Atsushi Nakanishi¹ · Koji Murakami¹

Received: 5 September 2018 / Accepted: 14 January 2019 / Published online: 1 February 2019
© The Japanese Society of Nuclear Medicine 2019

Abstract

Objective Whole-body dynamic imaging using positron emission tomography (PET) facilitates the quantification of tracer kinetics. It is potentially valuable for the differential diagnosis of tumors and for the evaluation of therapeutic efficacy. In whole-body dynamic PET with continuous bed motion (CBM) (WBDCBM-PET), the pass number and bed velocity are key considerations. In the present study, we aimed to investigate the effect of a combination of pass number and bed velocity on the quantitative accuracy and quality of WBDCBM-PET images.

Methods In this study, WBDCBM-PET imaging was performed at a body phantom using seven bed velocity settings in combination with pass numbers. The resulting image quality was evaluated. For comparing different acquisition settings, the dynamic index (DI) was obtained using the following formula: $[P/S]$, where P represents the pass number, and S represents the bed velocity (mm/s). The following physical parameters were evaluated: noise equivalent count at phantom (NEC_{phantom}), percent background variability ($N_{10\text{ mm}}$), percent contrast of the 10 mm hot sphere ($Q_{H, 10\text{ mm}}$), the $Q_{H, 10\text{ mm}}/N_{10\text{ mm}}$ ratio, and the maximum standardized uptake value (SUV_{max}). Furthermore, visual evaluation was performed.

Results The NEC_{phantom} was equivalent for the same DI settings regardless of the bed velocity. The $N_{10\text{ mm}}$ exhibited an inverse correlation ($r < -0.89$) with the DI. $Q_{H, 10\text{ mm}}$ was not affected by DI, and a correlation between $Q_{H, 10\text{ mm}}/N_{10\text{ mm}}$ ratio and DI was found at all the velocities ($r > 0.93$). The SUV_{max} of the spheres was not influenced by the DI. The coefficient of variations caused by bed velocity decreased in larger spheres. There was no significant difference between the bed velocities on visual evaluation.

Conclusion The quantitative accuracy and image quality achieved with WBDCBM-PET was comparable to that achieved with non-dynamic CBM, regardless of the pass number and bed velocity used during imaging for a given acquisition time.

Keywords Dynamic · PET · Continuous bed motion · Quantity · Whole-body

Introduction

Whole-body positron emission tomography (PET) uses the step-and-shoot (SS) technique and has been widely investigated. SS techniques necessitate the use of multiple overlapping beds (approximately ≥ 8 beds) to achieve uniform axial coverage of the patient [1–4]. However, these techniques entail long acquisition times because of overlapping bed positions. Continuous bed motion (CBM) acquisition has

been clinically available for commercial PET systems for several years. CBM techniques involve continuous movement of the patient bed, which helps in eliminating overlapping scans associated with SS [5–7]. The use of CBM techniques require the determination of bed motion velocity instead of acquisition time per bed as is done in the conventional SS techniques. In the previous studies, the image quality and quantitative data obtained with CBM were shown to be equivalent or better than those obtained with SS imaging with respect to image contrast, uniformity, and end-plane imaging [5–9]. In particular, quantitative studies that compared CBM and SS revealed no difference between mean standardized uptake values (SUV) calculated for phantom or clinical studies [7–11].

✉ Hideo Yamamoto
hyamamot@juntendo.ac.jp

¹ Department of Radiology, Juntendo University School of Medicine, 3-1-3, Hongo, Bunkyo-ku, Tokyo 113-8421, Japan

Several studies have demonstrated the quantitative benefits of dynamic PET; in addition, its protocol allows for the quantification of tracer kinetics, which plays an important role in tumor diagnosis and monitoring of therapeutic effect [12–18]. However, dynamic PET typically requires long scan times due to various issues specific to the SS technique, such as overlapping bed positions. As previously mentioned, the CBM technique does not require overlapping scans unlike the SS technique. Osborne et al. described that CBM-PET techniques using the standard whole-body dynamic imaging principles achieve expected quantitative results as compared to that achieved with the standard dynamic imaging methods and previously published values [19]. However, they only reported clinical data pertaining to patients and did not verify the physical parameters in a phantom study. PET is a quantitative imaging technique and requires a high quantitative accuracy [20–22]. Therefore, verification of physical parameters including the radioactivity concentration in a phantom study is important to ensure the quantity and quantification of whole-body dynamic imaging with CBM-PET. Dynamic PET technique using CBM (dynamic CBM) requires specific pass numbers and the bed velocity is two-to-ten times faster than that in non-dynamic CBM. To the best of our knowledge, the physical parameters of whole-body dynamic PET with CBM (WBDCBM-PET) using a phantom are not well characterized. This study investigates the impact of WBDCBM-PET on the quantification of summed images, without considering the quantification of the end-point kinetic parameters of dynamic PET. However, summed images obtained using the dynamic acquisition help in the improvement of the signal-to-noise ratio and the reduction of the variation of the pixel value, which are extremely important for clinical diagnosis. This study aimed to investigate the effect of a combination of pass numbers and bed velocity on the quantitative accuracy and quality of WBDCBM-PET images.

Materials and methods

Systems and imaging procedure

In this study, a WBDCBM-PET imaging system (Biograph mCT Flow 20-4R, Siemens Medical Solutions USA, Inc.) was used. A National Electrical Manufacturers Association (NEMA) body phantom containing six spheres (diameter, 10–37 mm) was used for the evaluation of the physical parameters and image quality. The background region of body phantom was filled with 4.22 kBq/mL of ^{18}F -fluorodeoxyglucose (FDG), and the six spheres were prepared with four times the concentration of the background region. Phantoms were made for each bed velocity and were scanned either the same or the different day. The

average radioactivity concentration of these phantoms was 42.91 ± 0.47 MBq. Image analyses were conducted using PETquact (Nihon Medi-physics, Tokyo) and Fusion Viewer Software (AZE, Tokyo). Non-dynamic CBM acquisition (single pass) with a bed velocity of 1 mm/s was performed to compare with dynamic CBM (multiple passes) acquisition. Imaging for WBDCBM-PET, which comprised six bed velocity settings (2–7 mm/s) in combination with pass numbers up to 21 and non-dynamic CBM, was performed on the NEMA body phantom (Fig. 1). We defined a dynamic index (DI) as a parameter of acquisition time on dynamic CBM, and this index facilitated the determination of bed velocity and the number of passes in WBDCBM-PET. The DI was obtained using the following formula: $[P/S]$, where P is pass number and S is bed velocity (mm/s). In this study, the scan duration of non-dynamic CBM was equivalent to that of WBDCBM-PET in DI 1, where P and S were 1 and 1 mm/s, respectively. Dynamic and non-dynamic CBM acquisitions were performed for 780 s and 260 s, respectively. The scan durations of DI 1, DI 2, and DI 3 were 260 s, 520 s, and 780 s, respectively. Prompt coincidence events in DI 1 accounted for approximately 46 Mcounts. Reconstructions were performed using time-of-flight (TOF) measurements, which have been used for clinical purposes in our hospital; pixel sizes in the axial plane and the direction of transverse axis were 4 and 2 mm, respectively. Iterative reconstruction employed a three-dimensional ordered subset expectation maximization (OSEM) algorithm with 3 iterations and 21 subsets. Point spread function (PSF) and attenuation correction were used, and post-filtering was applied using the Gaussian filter at 4 mm.

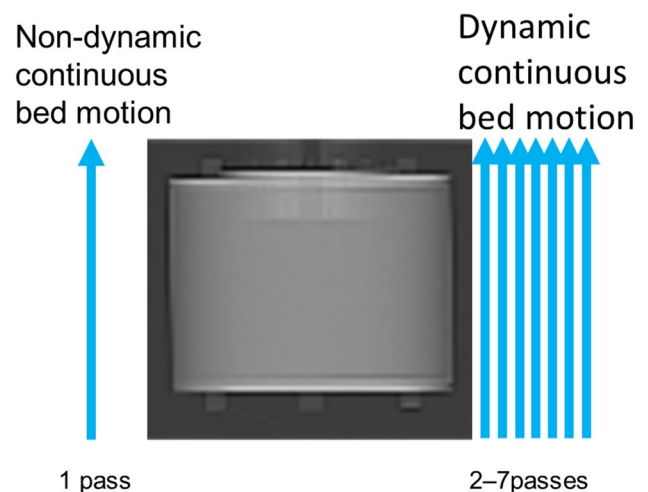


Fig. 1 Comparison between non-dynamic continuous bed motion (CBM) and dynamic CBM imaging of a National Electrical Manufacturers Association body phantom. Non-dynamic CBM was performed with 1 pass number and 1 mm/s bed velocity. Dynamic CBM was performed with pass numbers of 1–21 and bed velocity of 2–7 mm/s

Data analysis

The following physical parameters were evaluated: $NEC_{phantom}$, the percent background variability at 12 regions of interests (ROI) (diameter: 10 mm) set in the background area ($N_{10\text{ mm}}$), the percent contrast in the 10-mm-diameter hot sphere ($Q_{H,10\text{ mm}}$), the $Q_{H,10\text{ mm}}/N_{10\text{ mm}}$ ratio ($Q_{H,10\text{ mm}}/N_{10\text{ mm}}$), which represents the indicators of lesion detectability, and the maximum standardized uptake values (SUV_{max}).

$NEC_{phantom}$ was calculated using the following formula:

$$NEC_{phantom}(Mcounts) = (1 - SF)^2 \times \frac{(P - D)^2}{(P - D) + (1 + k)fD}, \quad k = 1,$$

where SF, k , and f represent scatter fraction, random scaling factor, and ratio of object size to the cross-sectional area of the imaging field of view, respectively. P and D represent the prompt and delayed coincidences, respectively [23].

$N_{10\text{ mm}}$ was calculated using the following formula:

$$N_{10\text{ mm}}(\%) = \frac{SD_{10\text{ mm}}}{C_{B,10\text{ mm}}} \times 100,$$

where $SD_{10\text{ mm}}$ is the standard deviation in a set of 12 10-mm-diameter ROIs on a background area with the six spheres visualized most clearly. Similar circular ROIs were also set for slices at distances of approximately ± 1 and ± 2 cm from the slice. $SD_{10\text{ mm}}$ is calculated as follows:

$$SD_{10\text{ mm}} = \sqrt{\frac{\sum_{k=1}^K (C_{b,10\text{ mm},k} - C_{B,10\text{ mm}})^2}{K - 1}}, \quad K = 60,$$

where $C_{b,10\text{ mm},k}$ is the 10-mm-diameter ROI in the background area and $C_{B,10\text{ mm}}$ is the average value of all background 10-mm-diameter ROIs [23].

$Q_{H,10\text{ mm}}$ was calculated using the following formula:

$$Q_{H,10\text{ mm}}(\%) = \frac{\left(\frac{C_{H,10\text{ mm}}}{C_{B,10\text{ mm}}} - 1\right)}{\left(\frac{\alpha_H}{\alpha_B} - 1\right)} \times 100,$$

where $C_{H,10\text{ mm}}$ is the average value of 10-mm spheres. α_H/α_B is the activity concentration ratio for the hot sphere to background [23]. The influence due to the difference in DI was verified using these physical parameters and was compared with those of non-dynamic CBM. These physical parameters were verified using statistical analysis and coefficient of variation (CV). In addition, the $N_{10\text{ mm}}$, $Q_{H,10\text{ mm}}$, and $Q_{H,10\text{ mm}}/N_{10\text{ mm}}$ were compared with and without PSF to confirm the influence on these metrics due to pixel values, which were enhanced by PSF in DI 1 measurements.

Furthermore, visual evaluation of the slices, in which all spheres were clearly visible among seven bed velocities in

DI 1, was performed using Scheffe’s method of paired comparisons (Nakaya’s variation) at a significant level of 0.05. Evaluation criteria comprehensively included the assessment of the background noise and the depiction of six spheres by six individuals using the five-point scale. Statistical analyses were conducted using R version 3.3.0 (R Core Team 2016) and BellCurve for Excel version 2.15 (Social Survey Research Information Co., Ltd., Tokyo).

Results

The $NEC_{phantom}$ was constant for the same DI settings regardless of the bed velocity (Fig. 2), and the CV was 2.2%. No significant differences were observed between single and multiple passes CBM with respect to the $NEC_{phantom}$ values; the percent difference ranged from –4.4 to 1.6%. Figure 3a shows the relationship between $N_{10\text{ mm}}$ and DI. Increase in DI led to a decline in $N_{10\text{ mm}}$, and a strong correlation ($r < -0.89$, $p < 0.05$) was observed at each velocity. The $N_{10\text{ mm}}$ in DI 1 was nearly the same as that in non-dynamic CBM. The CV of the $N_{10\text{ mm}}$ in DI 1, 2, and 3 were 7.5%, 14.1%, and 10.8%, respectively. The $Q_{H,10\text{ mm}}$ values were not dependent on DI, and there was no significant difference ($P = 0.816$) between $Q_{H,10\text{ mm}}$ at the different DI indices tested. In addition, no difference was noted regarding the $Q_{H,10\text{ mm}}$ between single and multiple passes CBM at all velocities (Fig. 3b). The CV of the $Q_{H,10\text{ mm}}$ in DI 1, 2, and 3 were 17.0%, 11.8%, and 14.2%, respectively, although the $N_{10\text{ mm}}$ was strongly correlated with DI, the $Q_{H,10\text{ mm}}$ was not influenced by DI. Consequently, the $Q_{H,10\text{ mm}}/N_{10\text{ mm}}$ improved with increasing DI, and a strong correlation between $Q_{H,10\text{ mm}}/N_{10\text{ mm}}$ and DI was observed at all bed velocities ($r > 0.93$, $p < 0.005$)

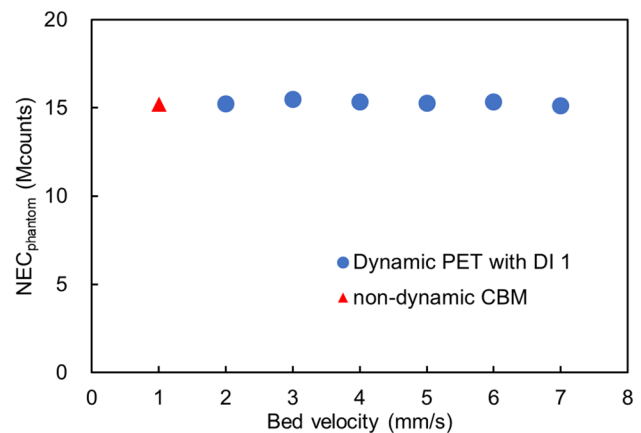


Fig. 2 Relationship between bed velocities and the $NEC_{phantom}$ in dynamic index 1 and comparison between non-dynamic and dynamic CBM considering $NEC_{phantom}$ values; $NEC_{phantom}$, noise equivalent count at phantom

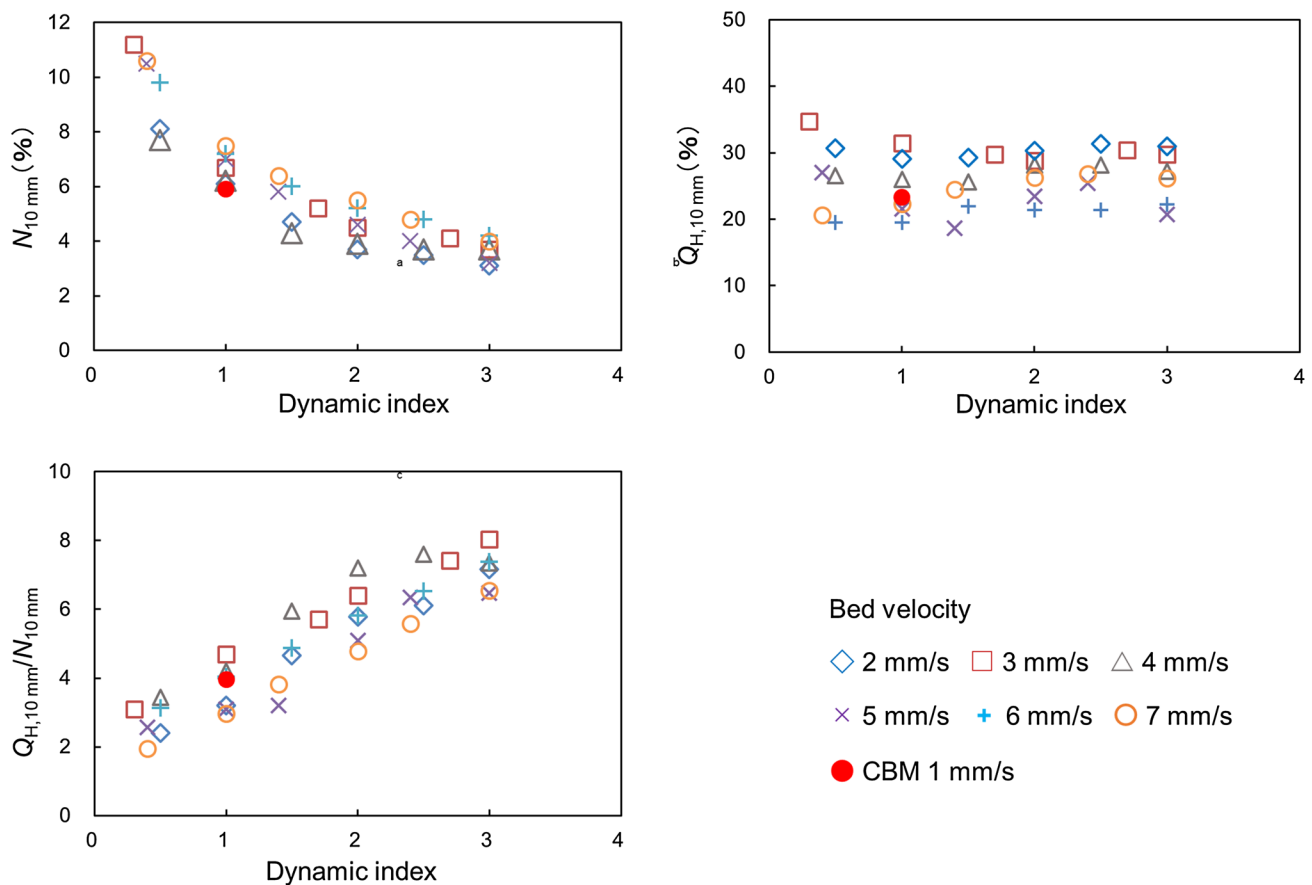


Fig. 3 Relationship between dynamic index and **a** $N_{10\text{ mm}}$, **b** $Q_{H,10\text{ mm}}$, and **c** $Q_{H,10\text{ mm}}/N_{10\text{ mm}}$ ratio and comparison between non-dynamic and dynamic CBM regarding these values in dynamic index 1.

(Fig. 3c). The CV of $Q_{H,10\text{ mm}}/N_{10\text{ mm}}$ in DI 1, 2, and 3 were 17.4%, 13.7%, and 7.5%, respectively. The $N_{10\text{ mm}}$ with and without PSF was 6.1–7.5% and 5.8–7.1%, respectively, and $N_{10\text{ mm}}$ increased by an average of 3.4% by PSF. The $Q_{H,10\text{ mm}}$ with and without PSF was 19.5–31.4% and 19.0–24.9%, respectively, with an average increase rate of 25.0% by PSF. The $Q_{H,10\text{ mm}}/N_{10\text{ mm}}$ with and without PSF was 3.7–4.7 and 2.9–4.2, respectively, with an average increase rate of 7.9% by PSF. Different trends were not observed in all the velocities for these parameters with and without PSF. The relationship between the SUV_{max} and the DI at each sphere is presented in Fig. 4. The SUV_{max} at each sphere was not influenced by the DI, and these were almost equal to those in non-dynamic CBM. The CV of the SUV_{max} between the bed velocities ranged 3.3–11.2% and was lower for larger spheres. On visual evaluation, the image for 7 mm/s appeared more as Gibbs artifact compared with images from the other velocities (Fig. 5). However, 95% confidence interval between each image did not include 0, and the difference of average preference degree of each image did not exceed the Yardstick score

$N_{10\text{ mm}}$, percent background variability at 10-mm circular regions of interests; $Q_{H,10\text{ mm}}$, percent contrast of the 10-mm hot sphere

($Y_{0.05} = 0.39$). Hence, there was no significant difference between images obtained at the different seven bed velocities in statistical analysis.

Discussion

In this study, we performed a quantitative assessment of WBDCBM-PET using a phantom. It is well known that NEC has been used to evaluate the PET image quality and characteristics of the system [24]. As previously reported, CBM bed velocity derived from an NEC-based conversion table can be reliably used to determine the condition associated with equivalent image quality between CBM and SS acquisition methods [7, 11]. In this study, NEC of dynamic CBM was not impacted by bed velocity for DI equal to 1 and was approximately equal to that of non-dynamic CBM. NEC is constant for the overall acquisition time and is proportional to the overall acquired coincidence events. Therefore, the detection capability of coincidence events in dynamic CBM is equivalent to that in non-dynamic CBM and SS for a given

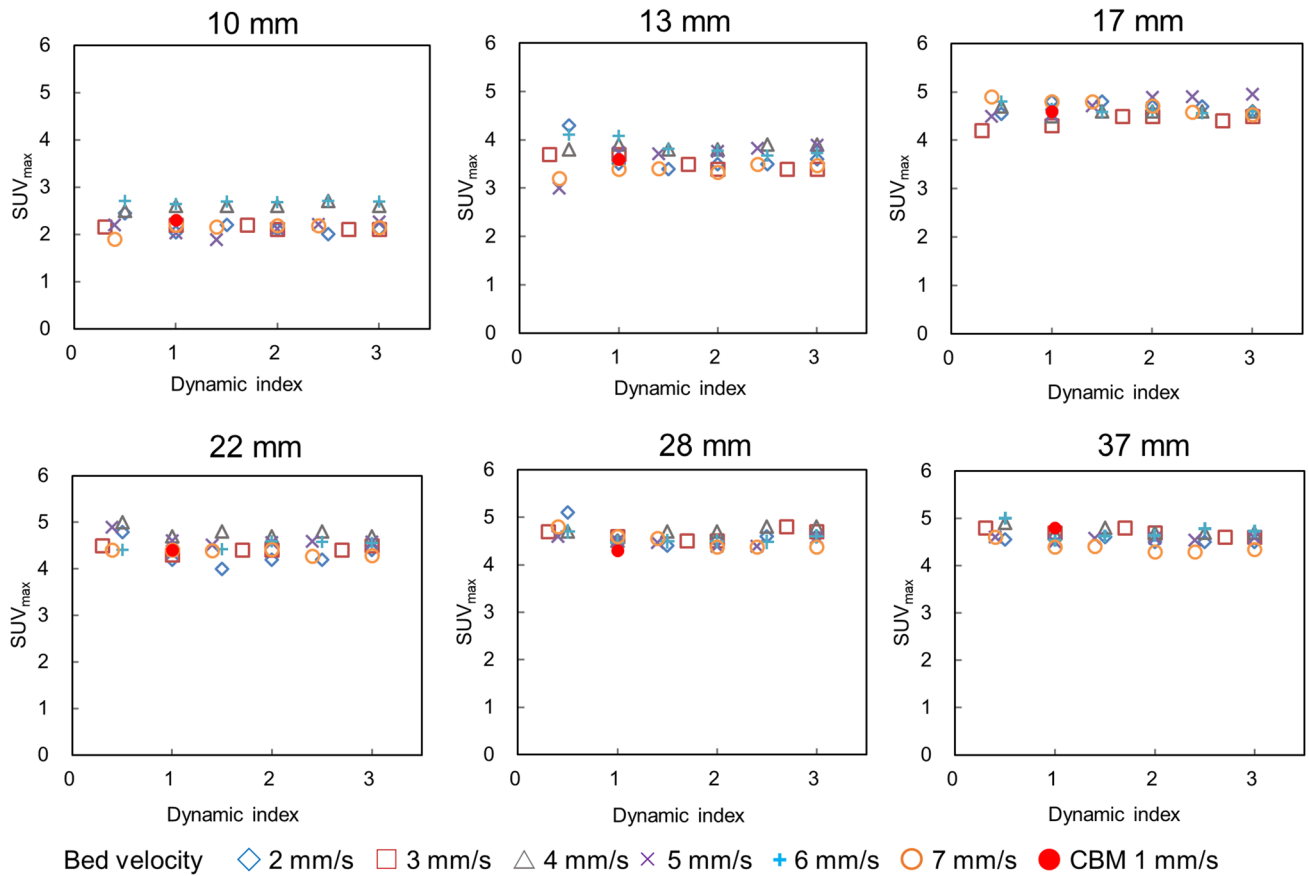
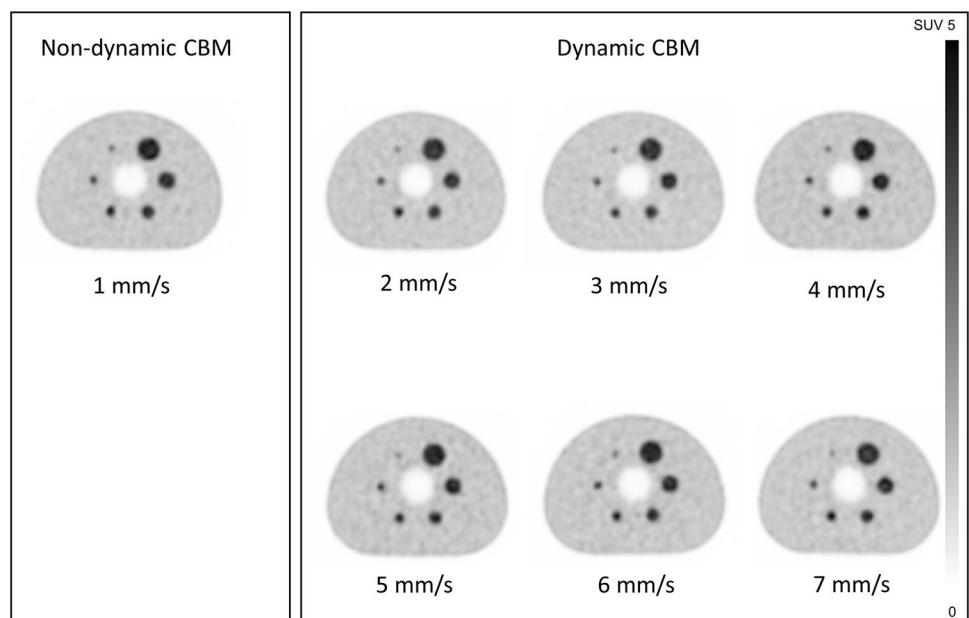


Fig. 4 Relationship between the SUV_{max} and the dynamic index at six spheres and comparison between non-dynamic and dynamic CBM regarding the specified values in dynamic index 1; SUV_{max} , maximum standardized uptake value

Fig. 5 Comparison of whole-body dynamic PET images obtained with continuous bed motion at seven bed velocities. *PET* positron emission tomography



acquisition time; in addition, the impact of NEC on image quality with dynamic CBM is equivalent to that with CBM or SS acquisition. $N_{10\text{ mm}}$ is an indicator of statistical noise [23], and an increasing DI means extension of acquisition time. In a study by Osborne et al., noise assessments showed statistically significant improvement with use of CBM techniques [7]. Accordingly, decrease in $N_{10\text{ mm}}$ with increase in DI can be interpreted as decline in statistical noise due to the extended acquisition time. The $Q_{H,10\text{ mm}}$ is the percent contrast for 10-mm hot sphere in the positive image [23]. The $Q_{H,10\text{ mm}}$ did not depend on DI, and this finding suggests that it is not affected either by bed velocity or the pass number in CBM. The observed improvement in the $Q_{H,10\text{ mm}}/N_{10\text{ mm}}$ ratio with an increase in DI is attributable to the decline in $N_{10\text{ mm}}$. The SUV_{max} values were constant regardless of DI and the bed velocity for all spheres, and there was almost no difference between non-dynamic and dynamic CBM in this respect. These results suggest that the SUV_{max} is not influenced by pass number or bed velocity.

The Japanese guidelines for the oncological FDG-PET/CT data acquisition protocol recommend $NEC_{\text{phantom}} > 10.8$ Mcounts, $N_{10\text{ mm}} < 5.6\%$ and $Q_{H,10\text{ mm}}/N_{10\text{ mm}} > 2.8\%$ [23]. In this study, the NEC_{phantom} ranged 14.4–15.2 Mcounts, which achieved its recommendation value. The range of the $N_{10\text{ mm}}$ with and without PSF was unable reach the recommendation value. On the other hand, the $Q_{H,10\text{ mm}}/N_{10\text{ mm}}$ with and without PSF were above the minimum recommended value. It has been reported that TOF improves the signal-to-noise ratio [25–27] and PSF modeling dose resolution, and enhances contrast [25, 28]. On the other hand, PSF modeling significantly alters image noise properties and induces edge overshoot effect, which is referred to as the Gibbs artifacts [25, 29]. Lee et al. reported that the use of PSF modeling reconstruction algorithm improved spatial resolution by 45%, and the percent contrast was significantly better than that achieved with the conventional OSEM without PSF [28]. However, the noise level associated with use of PSF modeling reconstruction was higher than that with the other reconstruction algorithms [25, 29]. Our study involved the use of TOF and PSF modeling. Moreover, the increase rate of the $Q_{H,10\text{ mm}}$ with PSF was larger than that of the $N_{10\text{ mm}}$ with PSF. Therefore, it is evident that PSF improves the percent contrast rather than increasing the noise [30]. In our study, we observed slight variations between each physical parameter and bed velocities at the same DI; however, no specific trend was identified with respect to bed velocity. $N_{10\text{ mm}}$, $Q_{H,10\text{ mm}}$, and $Q_{H,10\text{ mm}}/N_{10\text{ mm}}$ ratio are calculated using the average pixel value for a small ROI of 10 mm, and SUV_{max} is obtained from the maximum activity concentration per pixel in a ROI. These physical parameters are subject to statistical variability due to the reduction in the number of pixels, and the noise is enhanced by PSF. In addition, since the phantoms were made for each bed velocity, it

is hard to achieve precisely identical activity concentrations in each one. For these reasons, the variations in physical parameters may also be related to the statistical variation of pixel value and minor differences of radioactivity concentration at each phantom.

On visual evaluation, no significant difference was observed between the seven bed velocities; however, the image obtained for 7 mm/s appears more as Gibbs artifact compared with images obtained for other velocities. Kidera et al. reported that edge artifacts in PET images reconstructed using the PSF algorithm increased with an increasing sphere-to-background ratio of radioactivity [31]. As mentioned above, the limitation of this study is that minor differences of radioactivity were involved. It is believed that these reasons lead to the appearance of Gibbs artifacts in the image obtained for 7 mm/s. However, a lack of significant difference on visual evaluation using statistical analysis indicates that dynamic CBM can provide sufficient image quality compared with non-dynamic CBM. Dynamic CBM can reduce the acquisition time required to image the whole body. Therefore, even if an examination is canceled midway, it is possible to create an image from partially collected data. Furthermore, time-activity-curve can be created using multiple passes, and kinetic analysis can be performed using multiple passes. Future studies should investigate WBD-CBM-PET in a clinical research setting.

Conclusion

We verified the quantitative accuracy and image quality achieved with WBDCBM-PET. Dynamic CBM can provide image quality equivalent to that achieved with non-dynamic CBM and SS with comparable quantitative attributes. The results of this study would contribute to kinetic analysis and diagnosis of cancer using PET.

Acknowledgements A part of this study was presented at the Annual Meeting of SNMMI in Philadelphia, USA, Jun 23, 2018. The authors declare that they have no conflict of interest. This study received no funding.

Compliance with ethical standards

Ethical approval This article does not contain any studies with human participants or animals performed by any of the authors.

References

1. Cutler PD, Xu M. Strategies to improve 3D whole-body PET image reconstruction. *Phys Med Biol*. 1996;41:1453–67.
2. Boellaard R, Oyen WJ, Hoekstra CJ, Hoekstra OS, Visser EP, Willemsen AT, et al. The Netherlands protocol for standardisation

- and quantification of FDG whole body PET studies in multi-centre trials. *Eur J Nucl Med Mol Imaging*. 2008;35:2320–33.
3. Daisaki H, Shinohara H, Terauchi T, Murano T, Shimada N, Moriyama N, et al. Multi-bed-position acquisition technique for deep inspiration breath-hold PET/CT: a preliminary result for pulmonary lesions. *Ann Nucl Med*. 2010;24:179–88.
 4. McKeown C, Gillen G, Dempsey MF, Findlay C. Influence of slice overlap on positron emission tomography image quality. *Phys Med Biol*. 2016;61:1259–77.
 5. Panin VY, Smith AM, Hu J, Kehren F, Casey ME. Continuous bed motion on clinical scanner: design, data correction, and reconstruction. *Phys Med Biol*. 2014;59:6153–74.
 6. Acuff SN, Osborne D. Clinical workflow considerations for implementation of continuous-bed-motion PET/CT. *J Nucl Med Technol*. 2016;44:55–8.
 7. Osborne DR, Acuff S, Cruise S, Syed M, Neveu M, Stuckey A, et al. Quantitative and qualitative comparison of continuous bed motion and traditional step and shoot PET/CT. *Am J Nucl Med Mol Imaging*. 2015;5:56–64.
 8. Owaki Y, Nakahara T, Shimizu T, Smith AM, Luk WK, Inoue K, et al. Effects of breathing motion on PET acquisitions: step and shoot versus continuous bed motion. *Nucl Med Commun*. 2018;39:665–71.
 9. Schatka I, Weiberg D, Reichelt S, Owsianski-Hille N, Derlin T, Berding G, et al. A randomized, double-blind, crossover comparison of novel continuous bed motion versus traditional bed position whole-body PET/CT imaging. *Eur J Nucl Med Mol Imaging*. 2016;43:711–7.
 10. Rausch I, Cal-Gonzalez J, Dapra D, Gallowitsch HJ, Lind P, Beyer T, et al. Performance evaluation of the Biograph mCT Flow PET/CT system according to the NEMA NU2-2012 standard. *EJNMMI Phys*. 2015;2:26.
 11. Yamashita S, Yamamoto H, Nakaichi T, Yoneyama T, Yokoyama K. Comparison of image quality between step-and-shoot and continuous bed motion techniques in whole-body (18)F-fluorodeoxyglucose positron emission tomography with the same acquisition duration. *Ann Nucl Med*. 2017;31:686–95.
 12. Karakatsanis NA, Lodge MA, Tahari AK, Zhou Y, Wahl RL, Rahmim A. Dynamic whole-body PET parametric imaging: I. Concept, acquisition protocol optimization and clinical application. *Phys Med Biol*. 2013;58:7391–418.
 13. Karakatsanis NA, Lodge MA, Zhou Y, Wahl RL, Rahmim A. Dynamic whole-body PET parametric imaging: II. Task-oriented statistical estimation. *Phys Med Biol*. 2013;58:7419–45.
 14. Zhu W, Li Q, Bai B, Conti PS, Leahy RM. Patlak image estimation from dual time-point list-mode PET data. *IEEE Trans Med Imaging*. 2014;33:913–24.
 15. Houshmand S, Salavati A, Hess S, Werner TJ, Alavi A, Zaidi H. An update on novel quantitative techniques in the context of evolving whole-body PET imaging. *PET Clin*. 2015;10:45–58.
 16. Karakatsanis NA, Casey ME, Lodge MA, Rahmim A, Zaidi H. Whole-body direct 4D parametric PET imaging employing nested generalized Patlak expectation-maximization reconstruction. *Phys Med Biol*. 2016;61:5456–85.
 17. Palard-Novello X, Blin AL, Bourhis D, Garin E, Salaun PY, Devillers A, et al. Comparison of choline influx from dynamic (18)F-Choline PET/CT and clinicopathological parameters in prostate cancer initial assessment. *Ann Nucl Med*. 2018;32:281–7.
 18. Taddio MF, Mu L, Keller C, Schibli R, Kramer SD. Physiologically based pharmacokinetic modelling with dynamic PET data to study the in vivo effects of transporter inhibition on hepatobiliary clearance in mice. *Contrast Media Mol Imaging*. 2018;2018:5849047.
 19. Osborne DR, Acuff S. Whole-body dynamic imaging with continuous bed motion PET/CT. *Nucl Med Commun*. 2016;37:428–31.
 20. Burger IA, Vargas HA, Apte A, Beattie BJ, Humm JL, Gonen M, et al. PET quantification with a histogram derived total activity metric: superior quantitative consistency compared to total lesion glycolysis with absolute or relative SUV thresholds in phantoms and lung cancer patients. *Nucl Med Biol*. 2014;41:410–8.
 21. Boellaard R, Delgado-Bolton R, Oyen WJ, Giammarile F, Tatsch K, Eschner W, et al. FDG PET/CT: EANM procedure guidelines for tumour imaging: version 2.0. *Eur J Nucl Med Mol Imaging*. 2015;42:328–54. <https://doi.org/10.1007/s00259-014-2961-x>.
 22. Maus J, Hofheinz F, Schramm G, Oehme L, Beuthien-Baumann B, Lukas M, et al. Evaluation of PET quantification accuracy in vivo. Comparison of measured FDG concentration in the bladder with urine samples. *Nuklearmedizin*. 2014;53:67–77.
 23. Fukukita H, Suzuki K, Matsumoto K, Terauchi T, Daisaki H, Ikari Y, et al. Japanese guideline for the oncology FDG-PET/CT data acquisition protocol: synopsis of Version 2.0. *Ann Nucl Med*. 2014;28:693–705.
 24. Strother SC, Casey ME, Hoffman EJ. Measuring PET scanner sensitivity: relating countrates to image signal-to-noise ratios using noise equivalents counts. *IEEE Trans Nucl Sci*. 1990;37(2):783–788.
 25. Akamatsu G, Ishikawa K, Mitsumoto K, Taniguchi T, Ohya N, Baba S, et al. Improvement in PET/CT image quality with a combination of point-spread function and time-of-flight in relation to reconstruction parameters. *J Nucl Med*. 2012;53:1716–22.
 26. Vandenberghe S, Mikhaylova E, D’Hoe E, Mollet P, Karp JS. Recent developments in time-of-flight PET. *EJNMMI Phys*. 2016;3:3.
 27. Hashimoto N, Morita K, Tsutsui Y, Himuro K, Baba S, Sasaki M. Time-of-flight information improved the detectability of sub-centimeter sphere using clinical positron emission tomography/computed tomography scanner. *J Nucl Med Technol*. 2018;46:268–73.
 28. Lee YS, Kim JS, Kim KM, Kang JH, Lim SM, Kim HJ. Performance measurement of PSF modeling reconstruction (True X) on Siemens Biograph TruePoint TrueV PET/CT. *Ann Nucl Med*. 2014;28:340–8.
 29. Ashrafinia S, Mohy-Ud-Din H, Karakatsanis NA, Jha AK, Casey ME, Kadrmas DJ, et al. Generalized PSF modeling for optimized quantitation in PET imaging. *Phys Med Biol*. 2017;62:5149–79.
 30. Rahmim A, Qi J, Sossi V. Resolution modeling in PET imaging: theory, practice, benefits, and pitfalls. *Med Phys*. 2013;40:064301.
 31. Kidera D, Kihara K, Akamatsu G, Mikasa S, Taniguchi T, Tsutsui Y, et al. The edge artifact in the point-spread function-based PET reconstruction at different sphere-to-background ratios of radioactivity. *Ann Nucl Med*. 2016;30:97–103.

Publisher’s Note Springer Nature remains neutral with regard to jurisdictional claims in published maps and institutional affiliations.